Article

Not peer-reviewed version

Nanostructural Characterization of Luminescent Polyvinyl Alcohol / Graphene Quantum Dots Nanocomposite Films

Dhanumalayan Elumalai , B. Rodríguez , G. Kovtun , P. Hidalgo , B. Méndez , S. Kalleemula , G. M. Joshi , M. T. Cuberes *

Posted Date: 8 November 2023

doi: 10.20944/preprints202311.0500.v1

Keywords: Polyvinyl Alcohol; Graphene Quantum Dots; Atomic Force Microscopy; Ultrasonic Force Microscopy; Friction Force Microscopy; Photoluminescence; X-Ray Difraction; Infrared Spectroscopy; Thermogravimetry; Differential Thermal Analysis

Article

Nanostructural Characterization of Luminescent Polyvinyl Alcohol/Graphene Quantum Dots Nanocomposite Films

E. Dhanumalayan [1,2], B. Rodríguez [3], G. Kovtun [1,4], P. Hidalgo [3], B. Méndez [3], S. Kalleemula [2], G. M. Joshi [1,5] and M. T. Cuberes [1,*]

[1] Department of Applied Mechanics and Project Engineering, Mining and Industrial Engineering School of Almaden, University of Castilla-La Mancha, Plaza Manuel Meca 1, 13400 Almadén, Spain
[2] Thin Films Laboratory, Center for Functional Materials, Vellore Institute of Technology University, Vellore, 632014, Tamilnadu, India
[3] Department of Physics of Materials, University Complutense of Madrid, Madrid 28040, Spain
[4] Institute of Magnetism NAS of Ukraine and MES of Ukraine, Blvd. Acad. Vernadsky 36-b, 03142 Kyiv, Ukraine
[5] Department of Engineering Physics and Engineering Materials, Institute of Chemical Technology Mumbai, Marathwada Campus, Jalna, India
* Correspondence: teresa.cuberes@uclm.es

Abstract: Polyvinyl Alcohol (PVA)/Graphene Quantum Dots (GQDs) polymer nanocomposite films have been prepared, and the relationship between their structural, thermal and nanoscale morphological properties, and their photoluminescent response, has been investigated. Although according to X-ray Diffraction (XRD), Fourier-Transform Infrared Spectroscopy (FT-IR) and Differential Thermal Analysis (DTA) the incorporation of GQDs does not significantly affect the percentage crystallinity of the PVA matrix, for a range of added GQD concentrations, Atomic Force Microscopy (AFM) showed the formation of islands with apparent crystalline morphology on the surface of the PVA/GQD films, with GQD presumably acting as a nucleating agent for island growth. The incorporation of GQD also led to the formation of characteristic surface pores with increased stiffness and frictional contrast, according to Ultrasonic Force Microscopy (UFM) and Frictional Force Microscopy (FFM) data. The photoluminescence (PL) spectra of the films were found to depend both on the amount of GQD incorporated and on the film morphology. For GQD loads > 1,2wt%, a GQD-related band was observed at ~ 1650 cm^{-1} in FT-IR, along with an increase in the PL band at lower energy. For a load of ~2wt% GQD, the surface morphology was characterized by extended cluster aggregates with lower stiffness and friction than the surrounding matrix, and the PL signal decreased.

Keywords: polyvinyl alcohol; graphene quantum dots; atomic force microscopy; ultrasonic force microscopy; friction force microscopy; photoluminescence; x-ray difraction; infrared spectroscopy; thermogravimetry; differential thermal analysis

1. Introduction

Graphene quantum dots (GQDs) are intriguing emerging materials among the carbon allotropes as they possess a nonzero band gap and present size-dependent properties. The latter are attributed to quantum confinement and edge effects. One of the main characteristics of GQDs is the luminescence property, emerging because of electron confinement in all the special dimensions [1–3]. Tunable properties of GQDs are achieved through synthesis processes by controlling their size and tailoring their emission characteristics. The synthesis routes of GQDs include several procedures such as chemical exfoliation, lithography, and hydrothermal method, where coal, graphene, graphene oxide and reduced graphene oxide are used as the source material. The aqueous dispersion of GQDs is enabled due to the oxygen functional groups present at their edges. The functionalization

 doi:10.20944/preprints202311.0500.v1

of GQDs also showed improved properties in tailoring the electrical and optical properties. The applications of GQDs are not limited to particular sector, as they are widely used in light emitting diodes (LED), LED displays, photovoltaic devices, bio-imaging, bio-sensors, and electrochemical sensors [4,5]. Liquid suspended GQDs are glowing under UV light and have UV excitation and PL emission depending on their size and properties. By introducing GQDs in a polymer system, one can prepare GQD based highly stable polymer composites with superior electrical and luminescent responses for wide range of applications [6,7].

Polyvinyl alcohol (PVA) is a unique synthetic polymer obtained by partial or complete hydrolysis of polyvinyl acetate (PVAc) by replacing the acetate group (CH_3COO) with the hydroxyl (–OH) group. The chemical structure of PVA favors the formation of hydrogen bonds and gives it a hydrophilic character. PVA is well known for its facility to form stable films, superior optical transparency, and high solubility in water. PVA has been highly researched for its ability as a biocompatible carrier for drug delivery applications in clinical studies, and for its biodegradable property [8,9]. For decades, various fillers have been incorporated into PVA films and their structure-property relationship has been investigated. GQDs have also been used as fillers in PVA matrices and the enhancement of their luminescence properties has been explored [2,10–22].

In this work, we have prepared PVA/GQD nanocomposites with varying GQD content from 0,4 up to 2,0%wt, and we have carried out a thorough study of their structural, thermal and morphological properties on the nanometer scale using X-ray Diffraction (XRD), Fourier-Transform Infrared spectroscopy (FT-IR), Thermogravimetry (TGA), Differential Thermal Analysis (DTA), and Atomic Force Microscopy (AFM)-based techniques, including Ultrasonic Force Microscopy (UFM) and Lateral Force Microscopy (LFM). The results have been correlated with the photoluminescent response of the nanocomposite films when excited with a 325 nm laser source. The photoluminescence (PL) spectra of the films were found to depend on both the amount of GQD incorporated and the film surface morphology, even in those cases where neither XRD, FT-IR nor DTA revealed significant structural changes.

2. Materials and Methods

2.1. Preparation of the PVA/GQD nanocomposite films

Polyvinyl alcohol (PVA) in granular form (MW 31,000–50,000,98–99% hydrolyzed) and Graphene Quantum Dots < 5 nm in diameter, with maximum emission between 435-450 nm, in aqueous solution with a concentration of 1 mg/mL, were purchased from Merck. For the preparation of the PVA/GQD nanocomposite films, a 6%wt stock solution of pure PVA was first prepared by dissolving PVA granules in distilled water under constant stirring at 90ºC until the complete dissolution. Next, various amounts of GQDs solution were added to the PVA stock solution to obtain mixed solutions with 0.4-2.0 weight percentage of GQD NPs relative to PVA (denoted as %wt GQD), and the resulting mixtures were further stirred at 60ºC for ~ 5 hours. Finally, the mixtures were poured into Petri dishes, labelled appropriately, and kept at room temperature for evaporation of excess water. In about 36 h, PVA/GQD films a few microns thick could be easily peeled off from the containers. Figure 1 illustrates the schematics of the pure PVA and the PVA/GQD nanocomposite films preparation procedure. When introducing the PVA/GQD nanocomposites in a UV chamber, an intense blue emission could be observed even for those films with the lowest GQD concentrations (see Figure 1).

Preprints (www.preprints.org) | NOT PEER-REVIEWED | Posted: 8 November 2023 doi:10.20944/preprints202311.0500.v1

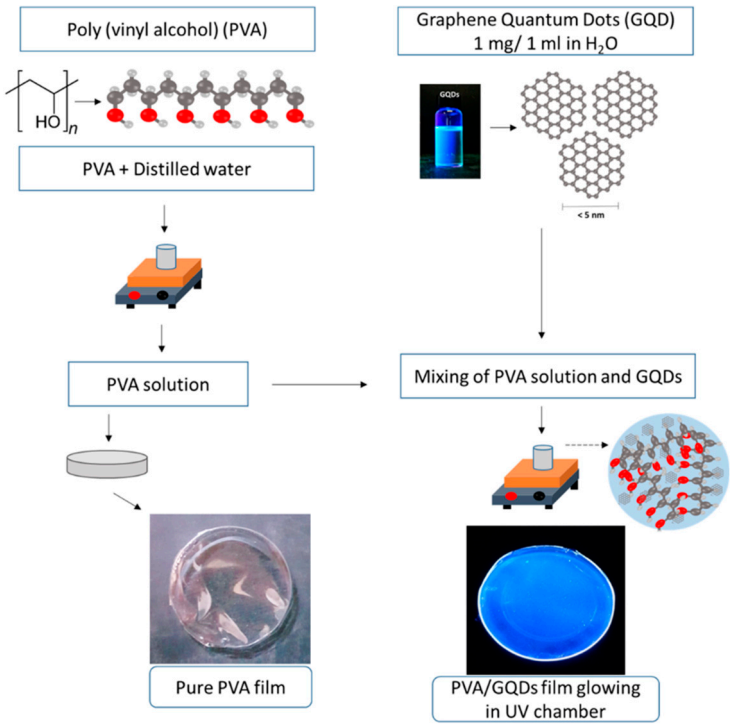

Figure 1. Schematics of the pure PVA and PVA/GQD nanocomposite films preparation procedure.

2.2. X-ray Difraction

X-ray Diffraction measurements were performed in an equipment Philips X'Pert MPD (Eindhoven, Holland), using CuK α radiation (1.54056 Å) with 40 KV and 40 mA. It incorporates 0.04 rad soller slits for both incident and diffracted beams, an automatic 12.5 mm programmable divergence slit, and a Xe gas sealed proportional detector. Data were collected in an angular range between 3° and 50° (2θ) with a step size of 0.02° and a counting time of 0.70 s per step. The data analysis was carried out with Origin software.

2.3. Fourier-Transformed Infrared Spectroscopy

FTIR spectra (4 cm^{-1} resolution, wavenumber range 500–4000 cm^{-1}) were recorded using a Shimadzu IRPrestige-21 spectrometer (Tokio, Japan), using the ATR method. Small pieces of the PVA/GQD nanocomposites hybrid films (≈ 10 μm thick) were cut and placed in the instrument sample holder. The data were acquired and analyzed using the software Shimadzu IR solution 1.21 (Tokio, Japan).

2.4. Thermogravimetry and Differential Thermal Analysis

Thermogravimetry and Differential Thermal analysis was carried out using a SETARAM model TG/DTA92 instrument (France) over the temperature range 30-500ºC with a heating rate of 5ºC/min in a Pt crucible in air atmosphere.

2.5. Scanning Probe Microscopy

Contact-mode atomic force microscopy (AFM), lateral force microscopy (LFM) and ultrasonic force microscopy (UFM) were performed using a NANOTEC (Madrid, Spain) instrument. The modification of the AFM equipment for the incorporation of UFM facilities is described in [23]. For UFM, ultrasonic frequencies of ~3.8 MHz and modulation frequencies of 2.4 KHz were applied from a piezoelectric element placed under the sample. Typically, Olympus Silicon Nitride cantilevers with a nominal spring constant of 0.06 N/m and a nominal tip radius of 20 nm were used. The

Preprints (www.preprints.org) | NOT PEER-REVIEWED | Posted: 8 November 2023 doi:10.20944/preprints202311.0500.v1

measurements were performed in air, at ambient conditions. Data analysis was performed with WSxM software (Madrid, Spain).

2.6. Photoluminiscence

Photoluminescence measurements were carried out at room temperature on a Horiba Jobin-Yvon LabRam Hr800 (Horiba, Kyoto, Japan) using a continuous wave He-Cd laser (λ = 325 nm). Different neutral filters were used to attenuate the total laser intensity, when necessary, diminishing the laser intensity from the nominal 5 mW. The laser was focused onto the sample surface using a 40 × objective (numerical aperture = 0.5, Thorlabs LMU-40X-NUV), which led to a laser spot diameter around 1 μm for the UV laser. The scattered light was collected with the same objective and dispersed with a grating of 600 L/mm and finally acquired with an air-cooled CCD detector Synapse.

3. Results and discussion

PVA exhibits semicrystalline properties due to inter- and intra-molecular hydrogen bonding (O–H) that provides the structural order of PVA chains [24,25]. Figure 2 shows the normalized XRD patterns of the pure PVA and PVA/GQDs composite films. The lowest black curve in Figure 2 corresponds to diffractogram of the pure PVA film. Within the considered angular range, four crystalline maxima at $\boldsymbol{2\theta \approx 16.1^{\circ}}$ indexed as (001), $\boldsymbol{2\theta \approx 19.4^{\circ}}$ $\boldsymbol{(10\bar{1})}$, $\boldsymbol{2\theta \approx 20.0^{\circ}}$ $\boldsymbol{(101)}$, **and** $\boldsymbol{2\theta \approx 22.7^{\circ}}$ $\boldsymbol{(200)}$, should be distinguished. The positions are indicated by arrows in Figure 2. Nevertheless, in our case, peaks at 19.4º and 20.0º were not resolved.

Considering a peak at $\boldsymbol{2\theta \approx 19.5^{\circ}}$ of FWHM of 2.1º, and applying the Debye-Scherrer equation,

$$\boldsymbol{D = \frac{K\lambda}{FWHM\ cos\theta}}$$

where *D* is the crystalline size, *K* the Scherrer constant (0,98), and $\boldsymbol{\lambda}$ the wavelength (0,154 nm), a size of $\boldsymbol{D \approx}$ 4.2 nm is estimated for the PVA crystallites, approximately the same as that of the GQD (nominal size < 5 nm).

The interplanar spacing may be estimated as $\boldsymbol{d \approx 4.5}$ Å taking into account Bragg's equation,

$$\boldsymbol{n\lambda = 2d(sin\theta)}$$

where *n* is the order of reflection.

The % of crystallinity was calculated as $\boldsymbol{\approx 18\%}$ by considering the ratio between the area of crystalline peaks and the total area in the XRD diffractogram.

Preprints (www.preprints.org) | NOT PEER-REVIEWED | Posted: 8 November 2023 doi:10.20944/preprints202311.0500.v1

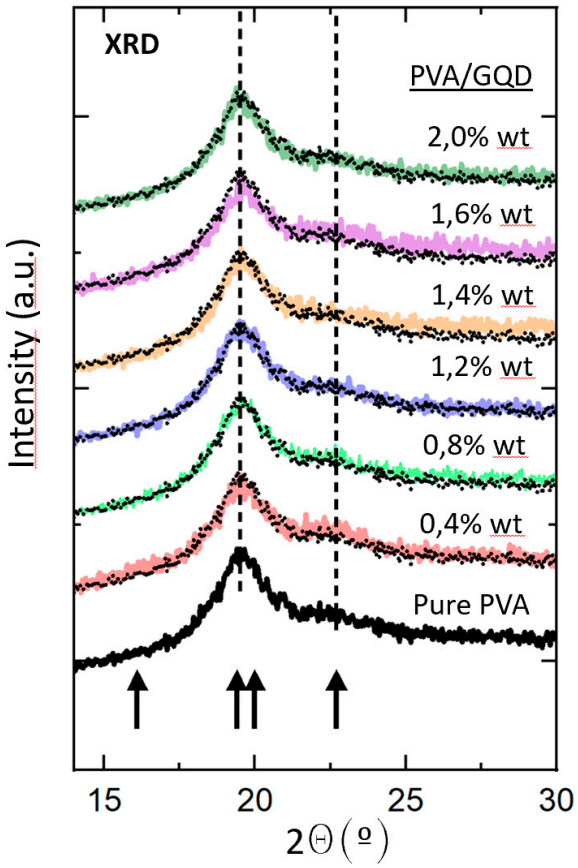

Figure 2. Normalized XRD patterns of the pure PVA and PVA/GQDs composite films. The dotted curve reproduces the diffractogram of the pure PVA film that has been superimposed on each of the diffractograms of the PVA/GQD nanocomposites with different GQD content, depicted in different colors for ease of comparison. The arrows indicate the position of expected maxima in crystalline PVA [24].

The normalized diffractograms of the PVA/GQD films with different GQD loadings correspond to the curves in different colors in Figure 2. In each case, the diffractogram of the pure PVA film has been superimposed (black dotted curve) on the corresponding curve for ease of comparison. As can be seen in Figure 2, the shape of the diffractogram does not undergo any significant change for the PVA/GQD films with the different %wt loadings of GQD. This fact indicates that neither the crystallinity percentage of the films nor the average size of the PVA crystalline domains should be significantly affected by the incorporation of GQD in our PVA/GQD nanocomposite films. Moreover, it is evident that no additional peak related to the presence of GQD is distinguished [26,27], even for the highest GQD load considered (2%wt).

The chemical structure of PVA/GQDs composite films has been analyzed with reference to the pure PVA film using FT-IR spectroscopy. Figure 3 shows the normalized FT-IR spectra for the pure PVA and PVA/GQD composite films. To characterize the FT-IR response of the GQD, a special sample was prepared by depositing a droplet of the GQD solution on a glass slide and waiting for 24 hours for the solvent to evaporate. The FT-IR spectra of the GQDs (on the glass slide) and of the clean glass slide without deposited GQDs are also shown in Figure 3.

Preprints (www.preprints.org) | NOT PEER-REVIEWED | Posted: 8 November 2023 doi:10.20944/preprints202311.0500.v1

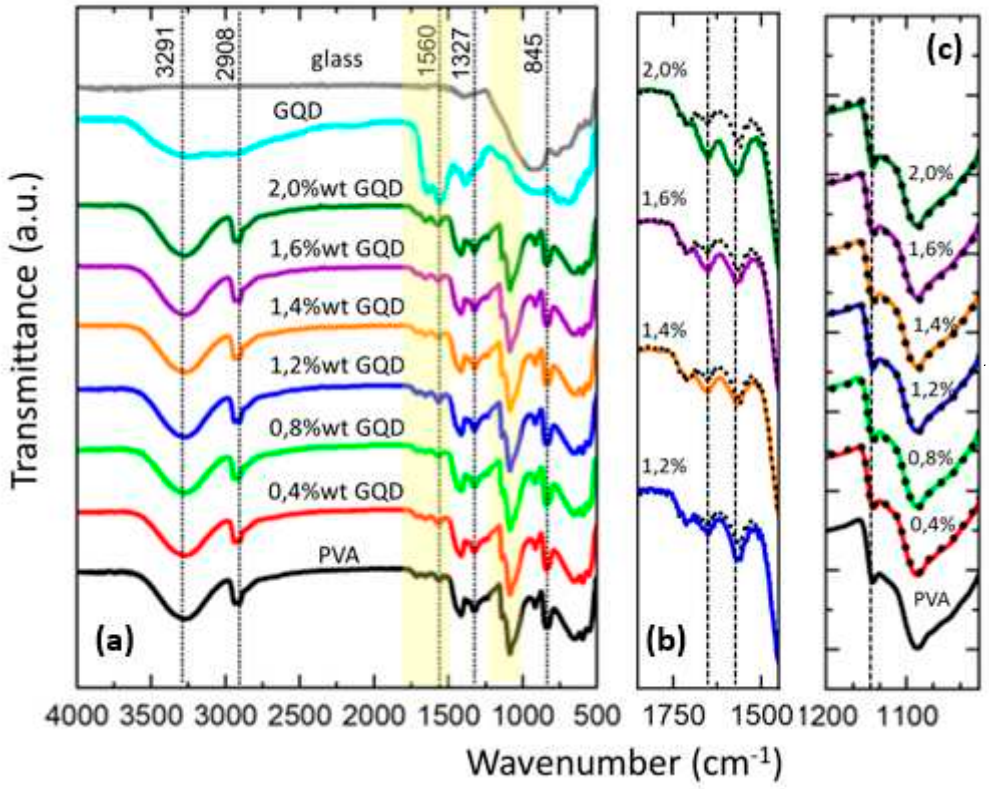

Figure 3. Normalized FT-IR spectra of the pure PVA and PVA/GQD composite films. (a) The FT-IR spectrum of GQD deposited on a glass slide (cyan curve) and of the clean glass slide (grey curve) is included. (b) (c) Zoom of the regions highlighted in yellow in (a). The dotted black curve corresponds to the FT-IR spectrum of pure PVA which has been shifted and superimposed on each of the other PVA/GQD film's FT-IR spectra for ease of comparison.

In Figure 3a, the broad band in the range of 3600 cm^{-1} to 3100 cm^{-1} is attributed to –OH stretching as a result of inter- and intra-molecular hydrogen bonding of PVA. An –OH band around the same range does also appears in the GQD spectrum. However, in the spectra of the PVA/GQD films no significant modification of the -OH peak with respect to the spectrum of the pure PVA is apparent, neither in shape nor in position of the maximum. For the highest GQD loads, a slight shift of the OH band maximum to higher wavenumbers can be allocated (by ~10 cm^{-1} for the %2wt GQD load, almost inappreciable in Figure 3a) possibly due to the incorporation to the GQD to the PVA matrix.

The peaks at 2935 cm^{-1} and 2908 cm^{-1} are assigned to the symmetric and asymmetric CH_2 stretching modes, and their shape and position remain the same for the pure PVA and the different PVA/GQD composites.

In the spectrum of GQD (cyan curve in Figure 3a), bands appear at 1650 cm^{-1} and 1560 cm^{-1}; however, these bands, although weak, are also found in the pure PVA and the PVA/GQD films. In pure PVA, the band at ~1654 cm^{-1} has been attributed to absorbed water [28,29]. Given the fact that the GQD sample was prepared from an aqueous solution, it is plausible that some water molecules remain attached to the GQDs after the evaporation of the solvent and give rise to this band. In the case of GQDs, such a band has been previously assigned to in-plane stretching vibration of the sp^2 hybridized C=C bond [30]. According to our data, it is clear that in our case, this peak can be associated with the presence of GQDs. The peak at 1560 cm^{-1} is attributed to C=O stretching [31]. Although our PVA was completely hydrolyzed (98 to 99%), some residual acetate groups in the PVA molecular chains contain carbonyl bonds that may explain the weak peak observed at ~1560 cm^{-1} in pure PVA and PVA/GQD films. In addition, GQDs are expected to have attached surface carboxyl groups (–COOH), with characteristic absorption band around 1566 cm^{-1} [30] and 1570 cm^{-1} [32].

 doi:10.20944/preprints202311.0500.v1

The modification of the PVA/GQD FT-IR spectra in the spectral region from 1850 to 1450 cm^{-1} is carefully investigated in Figure 3b. There, the FT-IR spectrum of pure PVA (black dotted curve in Figure 2b) has been superimposed on the spectra of PVA/GQD with different GQD loadings. For less than 1,2% wt GQD, no appreciable difference can be distinguished between the pure PVA and PVA/GQD spectral curves. However, for 1,2%wt GQD a slight increase in the bands coincident with those of the GQDs (cyan curve in Figure 3a) is seen, and the increase becomes larger as the amount of GQD incorporated into PVA matrix increases.

In Figure 3), the peaks around 1417 cm^{-1} and 1327 cm^{-1} are assigned to –OH bending (in-plane) and C–H wagging modes of PVA [33]. These peaks also remain identical in shape and position for the different PVA/GQD composites.

Particularly interesting is the peak at 1141 cm^{-1}, attributed to C-O/C-C stretching modes, which is typically used to evaluate the crystallinity of PVA using FT-IR analysis [29,34,35]. The FT-IR spectra of the pure PVA and PVA/GQD composites in the spectral region from 1200 to 1019 cm-1 are carefully investigated in Figure 3c. There, the FT-IR spectrum for pure PVA (black curve) has been vertically shifted and superimposed (black dotted curves) on the spectra of PVA/GQD with different GQD loadings. As can be seen in Figure 3c, the spectral curves do not change in shape or position as the amount of GQD incorporated into the PVA matrix increases. These results confirm the XRD observations that the percentage crystallinity of pure PVA is not affected by the GQD loading.

Eventually, in Figure 3a, the peaks at 1089 cm^{-1}, 916 cm^{-1} and 845 cm^{-1} are attributable to the C–O stretching, CH_2 rocking mode and C-C stretching vibrational modes respectively [36,37], which do not undergo any modification in shape or position in the pure PVA films and PVA/GQD composites. Table 1 lists the peak assignments discussed in the FT-IR spectra of Figure 3.

Table 1. Peak assignment in the FT-IR spectra in Figure 3.

FT-IR Wavenumber (cm^{-1})	Peak Assignment
3600 – 3100	O–H (stretching)
2935	CH_2 (symmetric)
2908	CH_2 (asymmetric)
1650	absorbed water/GQD
1560	C=O/COOH
1417	–OH (bending)
1327	C–H (wagging)
1141	C–O/C–C (stretching)
1089	C–O (stretching)
916	CH_2 (rocking)
842	C–C (stretching)

The thermal stability and thermal transition properties of the PVA/GQDs samples were studied over a varying temperature range by TG/DTA analysis. Figure 4 shows (a) TGA thermographs, (b) Differential-Thermogravimetry (DTG) curves and (c) (d) Differential Thermal analysis (DTA) data of pure PVA and PVA/GQD composite films.

Preprints (www.preprints.org) | NOT PEER-REVIEWED | Posted: 8 November 2023 doi:10.20944/preprints202311.0500.v1

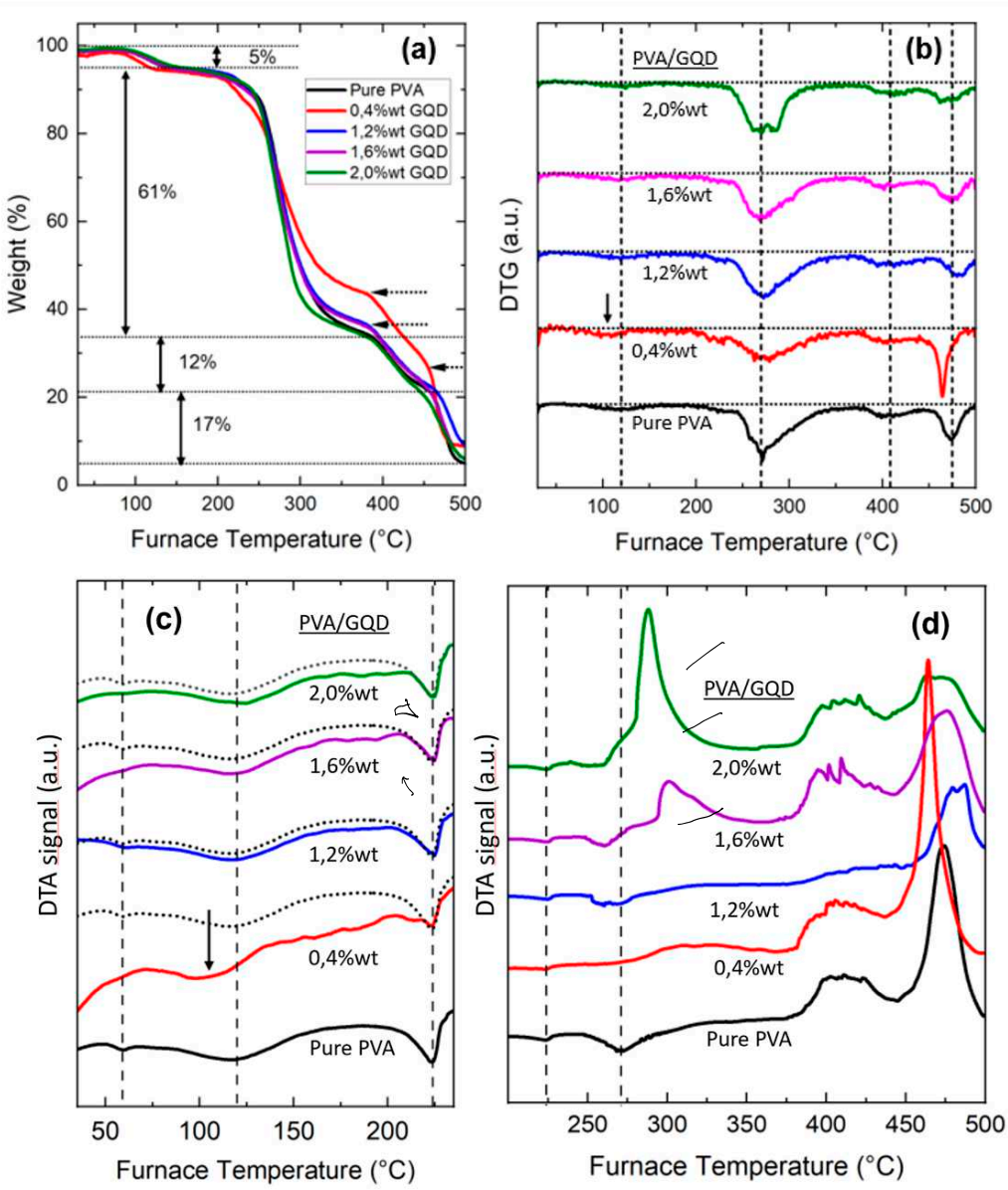

Figure 4. (a) TGA thermographs, (b) DTG curves and (c) (d) DTA data of pure PVA and PVA/GQD composite films.

From Figure 3a,b, four degradation phases can be distinguished. The percentage weight loss of each thermal degradation phase for PVA is indicated in Figure 4a. As can be seen in Figure 4, the inclusion of GQD in the PVA matrix influences the thermal behavior of the resulting nanocomposite film. Table 2 indicates the weight loss percentage for each degradation stage (measured from Figure 4a) and the % remaining at 500ºC.

Table 2. Weight loss percentage for each degradation step.

Weight loss %	Stage I	Stage II	Stage III	Stage IV	*Remains (500ºC)*
Pure PVA	5	61	12	17	5
0,4%wt GQD	5	51	17	18	9
1,2%wt GQD	5	58	15	12	10
1,6%wt GQD	5	58	15	15	7
2,0%wt GQD	5	61	12	15	7

 doi:10.20944/preprints202311.0500.v1

At the first degradation stage, a ~ 5% loss of weight is observed at temperatures between 70° to 160 °C in all films, which can be attributed to the evaporation of residual water within the samples [10,38]. The maximum weight loss temperature occurs at ~120ºC in all cases, except for the film with 0,4%wt GQD content, where it occurs at a temperature ~ 15ºC lower (see arrow in Figure 4b).

Figure 4c,d show the Differential Thermal Analysis data. In Figure 4c, the dashed lines indicate the endothermic peaks corresponding to the glass transition temperature, at ~59ºC, the evaporation of the residual water, at ~120ºC , and the crystalline melting point, at ~224º C, of the pure PVA film [39]. The curve corresponding to pure PVA has been superimposed (black dotted curves) on the curves measured for the other PVA/GQD films. No significant modification of those points is seen for the different films, except in the case of 0,4%GQD, for which the evaporation of the residual water occurs at ~15ºC less than for the pure PVA film (see arrow in Figure 4c), in agreement with the observations in Figure 4a,b. Moreover, the enthalpy of fusion of the different composites -area under the endothermic peak corresponding to the melting transition- is apparently similar to that of the pure PVA film for the different PVA/GQD nanocomposites, in agreement with the XRD results indicating that the percentage of crystallinity remains the same, except perhaps for the case of 0,4% GQD, whose DTA curve exhibits a positive slope.

The second degradation stage takes place at temperatures between 200 and 350 °C (Figure 4a,b), and is attributed to the disruption of the intermolecular hydrogen bonding in PVA, with partial chain-stripping elimination reactions (removal of water, with the elimination of hydroxyl side-groups) and chain-scission reactions (formation of free radicals by PVA chain breakage), leading to the formation of polyenes as a result of the thermal degradation [40,41]. From Figure 4b, for pure PVA the maximum weight loss temperature at which the degradation occurs in this second stage is at ~270ºC, at which an endothermic peak appears in the DTA measurements for the pure PVA film (Figure 3d). Interestingly, the DTG curves (Figure 4b) also reveal a small transition at the temperature region corresponding to the melting point, at the onset of this second degradation stage both for the pure PVA and the PVA/GQD composites. Nevertheless, when analyzing the DTA curves at temperatures close to 270ºC (see the corresponding dashed line in Figure 4d), the response of the different composites is apparently rather different. For the cases of 1,2% and 1,6% GQD, the endothermic peak appears shifted to lower temperatures, although the maximum loss peak in Figure 4b remains at the same position. And for the higher GQD contents, i.e. 1,6% and 2,0% GQD, DTA reveals the occurrence of an exothermic transition at this temperature, and an even more significant exothermic peaks are measured within this temperature range (see Figure 4d). The results in Figure 4d evidence that the presence of GQD alters the reactions taking place during this second stage of PVA degradation.

Finally, regarding the third and fourth degradation steps, above 350 °C, reactions giving rise to exothermic peaks in TDA take place (see Figure 4d). At these stages, the occurrence of further degradation and carbonization of PVA backbone structure is expected [42].

Let us study the surface features of the PVA/GQD nanocomposite films. Figure 5 shows 3D representations of the topography measured by AFM of the pure PVA and PVA/GQD nanocomposite films prepared with different GQD concentrations. As it is apparent from Figure 5, the incorporation of GQD within the PVA matrix has a strong impact on the film topographic features. The surface of the pure PVA film (Figure 5a) is characterized by the presence of rounded, homogeneously distributed clusters, ~80 nm in diameter. The Root Mean Square (RMS) roughness in Figure 5a is 1,6 nm, the surface skewness is 0,1, and the kurtosis is 3,0. However, on the sample with 0,4%wt GQD (Figure 5b), the surface structural homogeneity has been severely disrupted; the RMS roughness is now 2,1 nm, the skewness -2,0 and the kurtosis 21,1. Surface pores are now more clearly visible on the surface, and the former cluster structures cannot be now resolved, having been replaced by a kind of extended stratified islands.

Preprints (www.preprints.org) | NOT PEER-REVIEWED | Posted: 8 November 2023 doi:10.20944/preprints202311.0500.v1

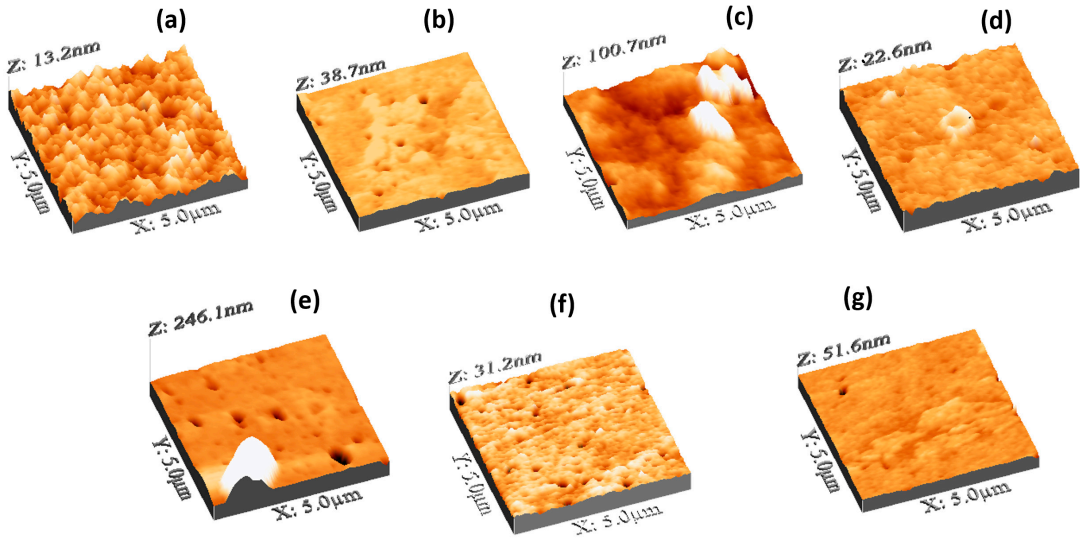

Figure 5. 3D representation of AFM topographic images recorded in contact mode for (a) pure PVA and PVA/GQD nanocomposite films with (b) 0,4% wt GQD, (c) 0,8%wt GQD, (d) 1,2%wt GQD, (e) 1,4%wt GQD, (f) 1,6%wt GQD, and (g) 2,0%wt GQD.

In the case of the sample with 0,8%wt GQD (Figure 5c), the changes are even more dramatic. Although XRD, FT-IR and DTA allows us to conclude that there is no variation on the percentage crystallinity of PVA for the films with different GQD concentrations, the AFM topographic image in this film clearly reveals the presence of 3D clusters with stepped walls and facets characteristic of a crystalline morphology. We attribute these features to the formation of crystalline PVA islands, possibly with GQD's acting as a nucleating agent for 3D crystalline PVA growth on the sample surface, as will be discussed in more detail below (see discussion related to Figure 7) In Figure 5c, the RMS roughness is 9,7 nm, the skewness 1,8 and the kurtosis 12.4.

On the film with 1,2%wt GQD (Figure 5d), the surface regains a flat appearance, with a surface roughness of 1,05 nm, a skewness of 0,1 and a kurtosis of 6,7. Pores and, in some cases, characteristic PVA annular structures at the rim of the pores may be observed.

On the film with 1,4%wt GQD (Figure 5e), 3D islands like those in Figure 5c were again found, together with pores similar to those in Figure 5d. Due to the presence of the 3D features and pores, the RMS roughness amounts to 12,5 nm, the skewness to 3,8 and the kurtosis to 18,4.

For the film corresponding to 1,6%wt GQD, in addition to (smaller) pores, small surface clusters aligned along a specific direction can be distinguished in Figure 5f. In this case, the RMS roughness is 1,4 nm, the skewness -1,3 and the kurtosis 12,17.

Eventually, for the case of 2,0%wt GQD, aligned surface clusters can be observed in Figure 5g, similar to those in Figure 5f, but gathered now to form larger aggregates. Here, the RMS roughness is 1,7 nm, the skewness -2,3 and the kurtosis 30,2.

In the following, characteristic features of the different PVA/GQD films will be discussed in more detail taking advantage of the application of different AFM modes, where relevant.

The images in Figure 6 were recorded on the PVA/GQD film with 0,4%wt GQD. Figure 6a shows the surface topography, recorded with contact-mode AFM. Figure 6b corresponds to a height-contour profile along the white line in Figure 6a. In the lower right-hand side of Figure 6a, the presence of a terrace ~ 4 nm higher is apparent. On the lower terrace, rounded clusters ~ 80 nm in diameter similar to those on the pure PVA sample surface can be distinguished; the area is characterized by frequent "void" defects possibly consisting in displaced clusters. There are also clusters on the upper terrace, although they do not have such a well-defined rounded shape. Figure 6c,d correspond to LFM images recorded over the area delimited by a dashed black rectangle in Figure 6a. As it is apparent from Figure 6c,d only a slight frictional contrast (darker in (c) and brighter in (d) over the same area) is noticeable at some areas over the higher terrace region, indicating a chemical homogeneity of the surface.

Preprints (www.preprints.org) | NOT PEER-REVIEWED | Posted: 8 November 2023 doi:10.20944/preprints202311.0500.v1

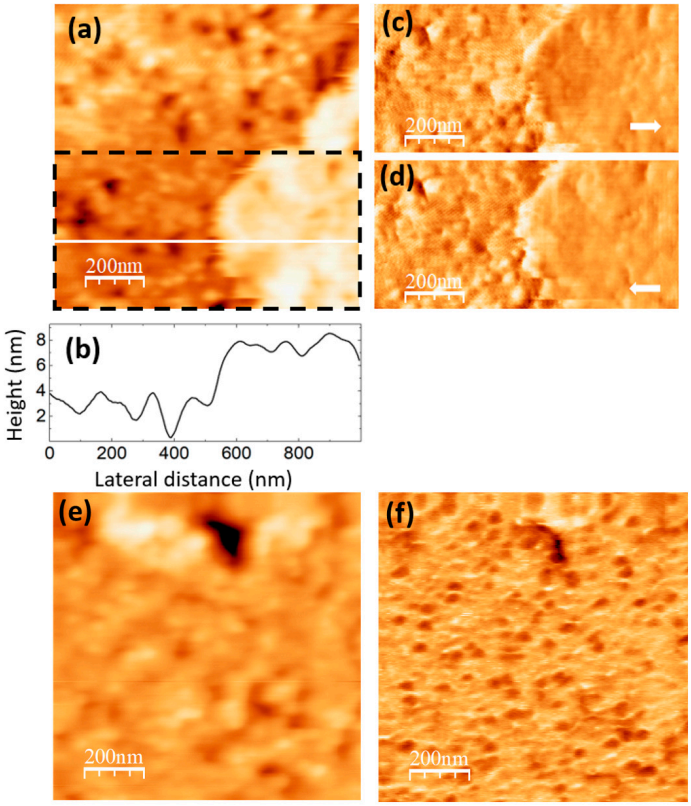

Figure 6. PVA/GQD film with 0,4%wt GQD. (a) Contact-mode AFM topography. Color-scale range: 12 nm (b) Height-contour profile along the white line in (a). (c) (d) LFM images recorded over the surface area enclosed by the dashed black rectangle in (a), scanning from left to right (c) and from right to left (d). (e) Contact-mode AFM topography over a different surface area than (a). Color-scale range: 12 nm. (f) UFM image simultaneously recorded with (e) over the same surface area.

Figure 6e,f correspond to contact-mode AFM topography (e) and UFM (f) images recorded over another surface area of the same sample. The UFM image reveals that some of the clusters topographically similar in (e) exhibit, however, a lower UFM contrast, indicative of a lower stiffness. Such result may arise from a different conformation and packing of the macromolecular PVA chains within such clusters, resulting in a lower density. Also, it is observed that the higher topographic area at the top in (e) does not lead to a notably different UFM contrast in (f), in agreement with conclusions obtained when analyzing Figure 6c,d.

The obtained results indicate that GQD interactions with PVA influence the conformation of the PVA chains with respect to those of pure PVA. GQDs can easily bind to a PVA chain via H-bonds through the chemical groups at their edges. According to the FT-IR data (see Figure 3a,b) our GQDs must contain groups with C=O bonds, as well as OH groups at their edges, which confers them hydrophilic nature. It is certainly plausible that they alter the conformation of the PVA chains when incorporated into the PVA matrix, promoting the formation of the void defects observed in Figure 6 (e) (i), and the re-arrangement of the PVA molecules into less dense clusters and/or new terraces. On the other hand, it is likely that these morphological changes facilitate water removal as observed by thermogravimetry for this film (see Figure 4a–c).

The images in Figure 7 were recorded on a PVA/GQD film with 0,8%wt GQD. Figure 7a,b correspond to contact-mode AFM (a) and UFM (b) images simultaneously recorded over a same surface area. As in Figure 5c, the topography reveals the formation of 3D islands of crystalline appearance. The fact that thin inorganic layered fillers may induce the crystallization of polymer nanocomposites is already well known [43]. It should be noted that those islands are much larger than the ~4,2 nm size estimated from the XRD data for the PVA crystalline domains, according to the Debye-Scherrer equation (see discussion related to Figure 2). The fact that XRD on this film does not

Preprints (www.preprints.org) | NOT PEER-REVIEWED | Posted: 8 November 2023 doi:10.20944/preprints202311.0500.v1

provide any indication of PVA crystal growth suggest that most probably their formation most likely occurs only on the film surface, whereas the XRD information comes not only from the surface, but from the whole PVA film. Furthermore, it could be the case that despite of the crystalline morphology of the islands, the specific domains in which the polymer atomic species are sufficiently well ordered to contribute to the XRD signal are much smaller than the island size.

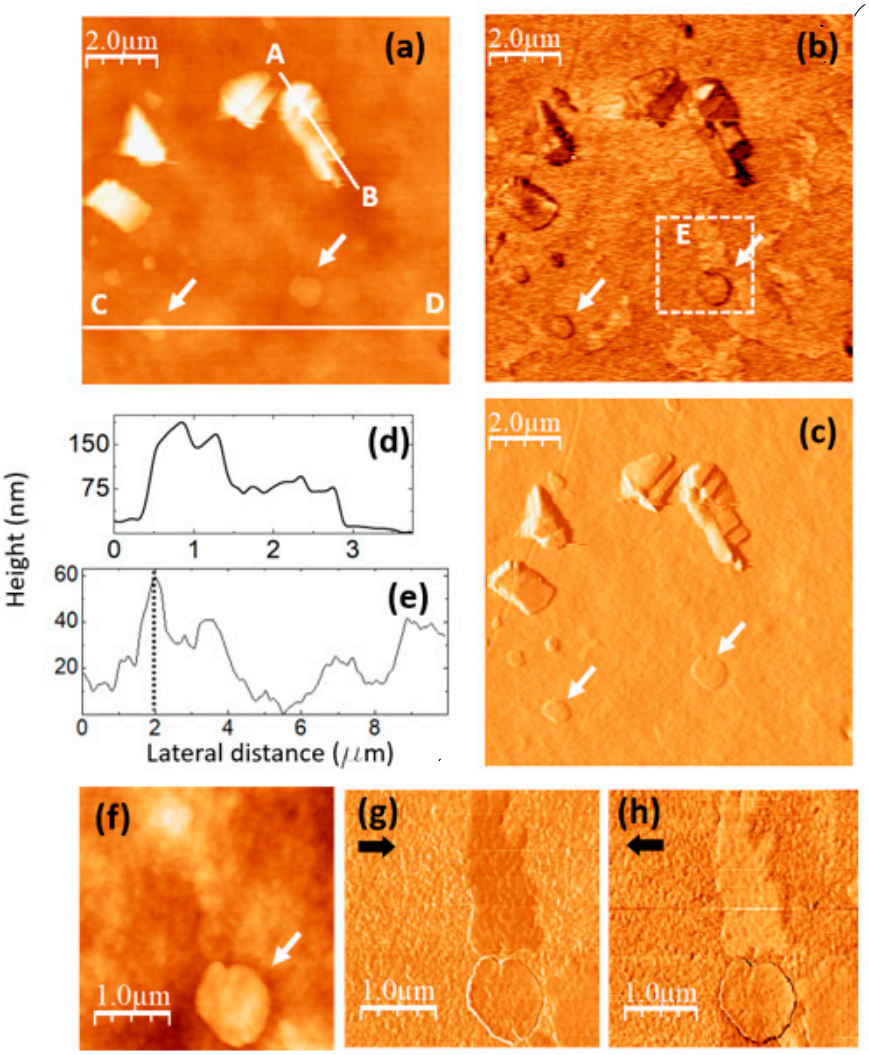

Figure 7. PVA/GQD film with 0,8%wt GQD. (a) contact-mode AFM image. Color-scale range: 208 nm (b) UFM image recorded simultaneously with (a), over the same surface area. (c) Derivative image of (a). (d) Height-contour profile recorded along the white line labelled A-B in (a). (e) Height-contour profile recorded along the lower white line labelled C-D in (a). (f) Contact-mode AFM image recorded over the area enclosed by the dashed white rectangle in (b). Color-scale range: 35 nm. (g) (h) LFM images recorded over the same surface area than (f) scanning from left to right (g) and from right to left (h).

The apparently crystalline 3D islands in Figure 7a are characterized by stepped facets with characteristic orientations and angles. Figure 7c corresponds to the derivative of the topography (Figure 7a) and has been included to facilitate the observation of topographic slope variations.

The islands contrast in UFM (Figure 7b) is facet-dependent, and it is probably strongly influenced by the orientation of the facet with respect to the tip. The chemical termination of the facet surface may also play an important role in the tip-sample adhesion, and thus in the resulting UFM signal.

Figure 7d shows the height-contour profile along the line A-B in Figure 7a, according to which the island height reaches ~ 180 nm; different island facets can be appreciated.

Preprints (www.preprints.org) | NOT PEER-REVIEWED | Posted: 8 November 2023 doi:10.20944/preprints202311.0500.v1

Next to those apparently crystalline islands, flatter rounded terraces can also be distinguished in Figure 7a, such as those marked with arrows. Figure 7e is a height-contour profile along the line C-D in Figure 7a that crosses one of these terraces. As can be seen in Figure 7c, the height of this terrace (indicated by a dashed line at the contour-profile curve) is ~ 58 nm, much higher than the terraces found on the PVA/GQD film with 0,4%wt GQD (see Figure 6). Those terraces are also distinguishable in the UFM image (Figure 7b), but they provide no distinct UFM contrast, apart from the originated from the slope changes at their edges.

Interestingly, in Figure 7b areas with a higher (brighter) UFM contrast are noticeable in the images at regions with no straightforwardly correlated topographic features, such as this labelled as "E". There is no correlation between the brightest UFM zones in Figure 7b and specific features in Figure 7a or c. Figure 7f–h correspond to topographic and LFM images recorded over the area within the dashed white rectangle in Figure 7b, scanning from right to left (g) and from left to right (h). A comparison of Figure 7b,g,h indicates that the stiffer areas in UFM (brighter contrast) exhibit lower friction (darker in (e) and brighter in (a)). Still, no clear correlation between the LFM images and the surface topography (Figure 7f) is noticeable for this area. This type of contrast may arise from the existence of buried PVA crystallite domains in the near subsurface region, positioned very close to the surface, thereby exerting an influence on the tip-sample frictional response. PVA crystals with stiffer contrast formed in the presence of an inorganic filler surface (sodium montmorillonite) have been previously observed using AFM modes [44].

Finally, it should be noticed that the aforementioned circular terraces (marked with arrows in Figure 7), do not show a significant frictional contrast in Figure 7g,h with respect to the substrate.

The images in Figure 8 were recorded on a PVA/GQD film with 1,2%wt GQD. Figure 8a,b correspond to simultaneously recorded contact-mode AFM topographic (a) and UFM (b) images; Figure 8c,d are also simultaneously recorded contact-mode AFM topographic (c) and UFM (d) images from another surface area of the same sample.

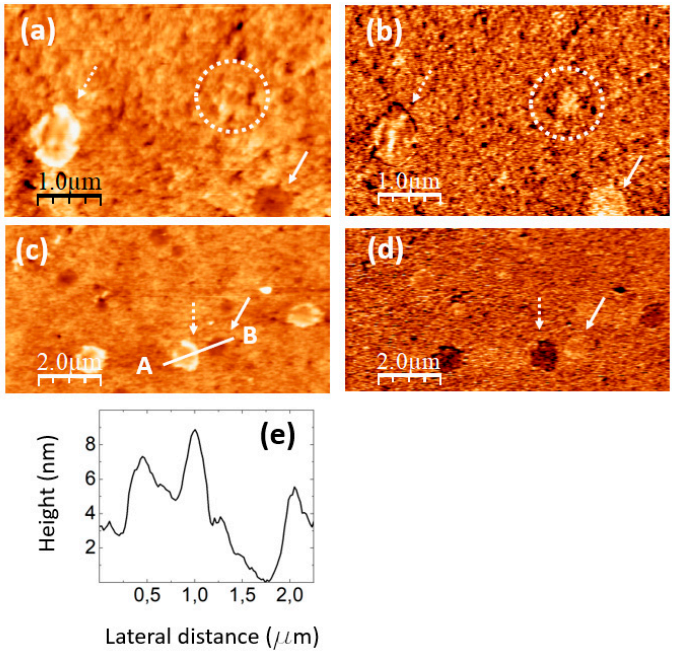

Figure 8. PVA/GQD film with 1,2%wt GQD. (a) Contact-mode AFM topography. Color-scale range: 14 nm. (b) UFM image recorded simultaneously with (a), over the same surface area. (c) Contact-mode AFM topography in a different area than (a). Color-scale range: 14 nm (d) UFM image recorded simultaneously with (c), over the same surface area. (e) Height-contour profile recorded along the lower white line in (c).

As can be seen in Figure 8a,c and Figure 5d, the incorporation of a higher amount of GQD (1,2%wt) leads to the formation of circular "pores" (e.g. those marked by continuous white arrows in

 doi:10.20944/preprints202311.0500.v1

Figure 8a,c) with various diameters, up to ~500 nm, and ~4 nm deep, some of them with a protruding ring at their edge (see Figure 5d also). In addition to the pores, circular structures with a surrounding annular rim are apparent (e.g. those marked by the dashed white arrows in Figure 8a,c). The internal diameter of such structures is ~ the same size as that of the pores, but their central area is larger than that of the substrate, their structure and origin being presumably common to those of the pores, but the latter being filled by additional molecules. In the circular structure marked by the dashed white arrow in Figure 8a, the rim is formed by clusters ~ 125 nm in diameter and ~ 5 nm in height; some cluster similar to those at the rim is also located over the central region.

Figure 8e shows a height-contour profile along the white line in Figure 8c from A to B that crosses one of the circular structures and a pore located nearby. Notice that the depressed central region of the circular structure is ~ 2 nm higher than the surrounding substrate.

In UFM (Figure 8b,d) the pores usually appear more rigid (brighter contrast). At some areas, such as the one enclosed by a dashed white circle in Figure 8a,b, the fact that the UFM image yields a stiffer contrast distinctly suggest that the topography corresponds to a covered pore area. Regarding the circular structure marked by the dashed white arrow in Figure 8c, the UFM (darker) contrast is clearly indicative of a softer zone. We understand this contrast has its origin in modified PVA clusters located both at the edge and filling the central part.

When analyzing Figure 5 (0,4%wt GQD loading), we observed defects which we termed “void” defects, that apparently consisted in displaced PVA surface clusters; we attributed the origin of those defects to the incorporation of a slight amount of hydrophilic GQDs into the PVA matrix, which incorporated to the PVA molecular chains via H bonding and influenced their conformation. For 1,2%wt GQD loading in Figure 8, we observe “pores”, much larger in diameter than the “voids”, which however could have a similar origin, but this time requiring a higher amount of GQDs to induce the modifications of the PVA molecular chains conformation, in which interactions of the GQDs with each other could also play a role.

The images in Figure 9 were recorded on a PVA/GQD film with 2,0%wt GQD. Figure 9a corresponds to the contact-mode AFM topography, Figure 9b is a height-contour profile along the white line in Figure 9a,c,d are LFM images recorded over the same surface area than Figure 9a scanning from right to left (c) and from left to right (d). Also, in this film, we find pores similar to those in Figure 8, such as this one marked by the continuous white arrow in Figure 9a, with a diameter of ~ 500 nm and depth of ~4 nm (see Figure 9b). At the pore zone, LFM reveals a higher frictional contrast (brighter in (c) and darker in (d)). According to Figure 9, for the 2,0wt% GQD load, the surface is characterized by the presence of cluster aggregates (e.g. this one marked by the dashed white arrow in Figure 9a), that yield a clear lower frictional contrast (Figure 9c,d).

Figure 9e,f correspond to contact-mode AFM topography and UFM image simultaneously recorded over the same surface area, different than this of Figure 9a, on the same sample. From the figures, it is noticeable that the aggregates in Figure 9a gather to form extended terraces, that yield a distinct softer (darker) UFM contrast, confirming that distinct phases characterized by different elastic and frictional contrast form on the film surface. It should be remarked that for GQD loading higher than 1,2%wt GQD, a GQD-related band emerges in the FT-IR spectrum (see Figure 3). We understand that the new PVA-GQD phase observed in Figure 9 develops as a result of the incorporation of GQD to the PVA molecular chains via H bonds, and the arrangement of the modified PVA molecules in a distinct conformation, which possibly also involves GQD-GQD interactions.

Preprints (www.preprints.org) | NOT PEER-REVIEWED | Posted: 8 November 2023 doi:10.20944/preprints202311.0500.v1

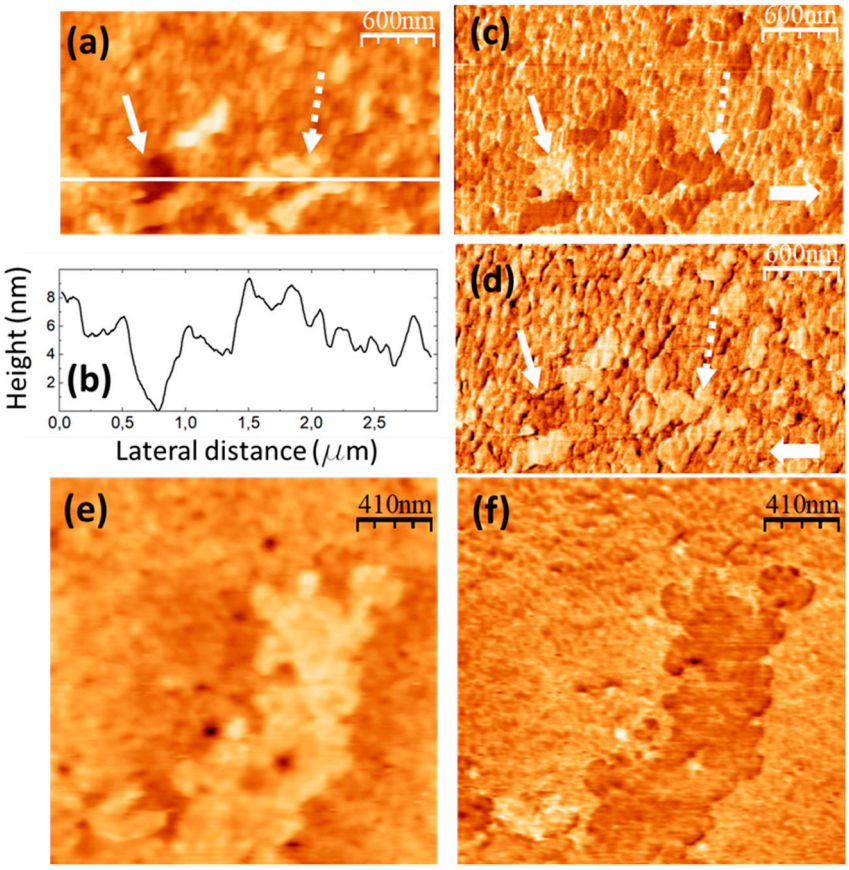

Figure 9. PVA/GQD film with 2,0%wt GQD. (a) Contact-mode AFM topography. Color-scale range: 12 nm. (b) Height-contour profile recorded along the lower white line in (a). (c) (d) LFM images recorded over the same area than (a) scanning from left to right (c) and from right to left (d). (e) Contact-mode AFM topography on a different surface area than (a). Color-scale range: 17 nm. (f) UFM image recorded simultaneously with (e), over the same surface area.

Figure 10 shows the PL spectra of the PVA/GQDs composite films. In PVA/GQD films, the PL response is due to the incorporation of the GQDs, and is excitation-dependent [10,12,14]. Our PL measurements were conducted at room temperature, utilizing a 325 nm laser source. As can be seen in Figure 10, the PL spectra of the PVA/GQD films exhibits maxima at ~420 nm, ~434 nm and ~495 nm (marked with dashed lines in Figure 10a,b). The PL emission intensity increases as the concentration of GQDs is increased, although in a nonlinear manner. In addition, the PL curves experience significant variations in shape that reflect that the relative contribution of each spectral component varies with the amount of GQD incorporated into the PVA matrix.

Preprints (www.preprints.org) | NOT PEER-REVIEWED | Posted: 8 November 2023 doi:10.20944/preprints202311.0500.v1

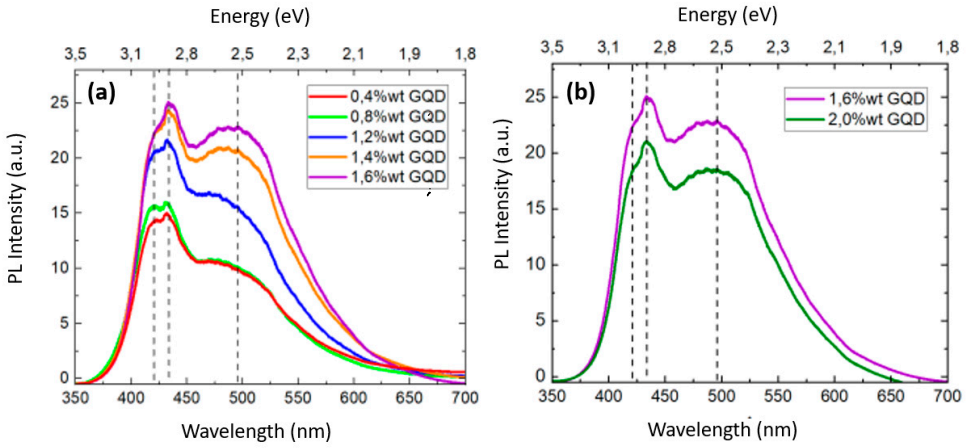

Figure 10. (a) Room temperature (RT) PL spectra of PVA/GQD films, obtained under 325 nm wavelength excitation, for the set of nanocomposites. (b) RT PL spectra of the composites with the two highest GQDs loads.

To date, there is still a need for a comprehensive understanding of the mechanisms behind the PL emission of GQDs [45,46]. There are three primary contributing factors: size, surface structure and edge effects. The quantum confinement effect of conjugated p-domains is determined by the carbon core. Surface states are determined by the hybridization of the carbon backbone and the connected chemical groups. Various functional groups (C–OH, C=O, O–C=O etc.) introduced during the growth of GQDs can give rise to surface states with energy levels located between the p and p* states of C=C, leading to the absorption/emission bands due to electron transitions within one or more of these groups. Both the edge structure and the presence of defects/surface states can significantly alter the electronic properties of GQDs. PL emission of GQDs primarily arises from the interplay between intrinsic state emission and defect state emission. Intrinsic state emission results from the quantum size effect, zigzag edge sites or the recombination of localized electron-hole pairs whereas defect state emission originates from energy traps.

Our PVA/GQD films, transparent under natural light, exhibited a bright blue color when placed inside a UV chamber (see Figure 1) even at the lowest considered GQD loads (0,4%wt GQD). An increase in GQD loading from 0,4 to 0,8%wt resulted in the growth of 3D islands on the PVA/GQD film surface (see Figures 5 and 7) but the PL response did not experience significant variations (see Figure 10a). This result suggests that when GQDs acting as nucleating agents for the growth of PVA crystallites, their PL response is quenched. However, for the 1,2%wt GQD load, a steady increase of the PL spectral response is observed. As the amount of incorporated GQD is further increased, the intensity of the PL band at lower energy (495 nm) increases, along with the emergence of the GQD-related band ~ 1650 cm^{-1} in FT-IR, while the higher energy PL band (maxima at ~420 and ~434 nm) reaches a saturation value. For ~2%wt GQD (Figure 10b), the overall PL spectral response decreases linearly. This decrease occurs when a new extended phase with clear and distinct elastic and frictional contrast is observed on the PVA/GQD film surface (see Figure 9), and hence could both events could be correlated.

Our results emphasize the impact of the surface molecular rearrangements and morphology on the PL response of PVA/GQD films. Further experiments are planned to explore the PL behavior in higher detail.

4. Summary and conclusions

Luminescent Polyvinyl Alcohol (PVA)/ Graphene Quantum Dots (GQDs) polymer nanocomposite films have been prepared with with varying GQD content ranging from 0.4 to 2.0

weight percentage of GQD NPs relative to PVA (%wt), and characterized using XRD, FT-IR, TGA, DTA, AFM, LFM, UFM, and PL spectroscopy.

XRD, FT-IR and DTA collectively indicate that the percentage crystallinity of the PVA film is not modified by the incorporation of GQDs into the matrix. For loads larger than 1,2%wt GQD, a GQD-related band is observed at ~ 1650 cm^{-1} in FT-IR.

According to the TGA results, for the film with 0,4%wt GQD, the maximum weight loss corresponding to the evaporation of the residual water occurs at about 15ºC lower temperature than in the pure PVA and the other PVA/GQD films. DTA reveals no significant modification of the films glass transition and melting point temperatures for the different GQD loadings, even though a markedly different degradation behavior is observed at temperatures above the melting point.

AFM reveals significant modifications of the film surface topography for the different GQDs loading. For 0,4%wt GQD, the topography is characterized by small "void" defects apparently formed by displaced PVA clusters, and surface terraces form, with no significant characteristic frictional or elastic contrast. At a GQD concentration of 0,8%wt, the film surface exhibits the formation of 3D islands with a typically crystalline morphology. This observation strongly indicates that the GQDs are likely serving as nucleating agents for PVA surface island growth. For 1,2%wt GQD the surface is characterized by "pores" up to ~500 nm in diameter, ~4 nm deep, that exhibit higher stiffness and friction contrast, as well as circular structures of similar diameter than the pores rimmed by clusters that yield lower stiffness and friction. For films with 2,0wt% GQD concentration, extended cluster aggregates with distinctly lower friction and stiffness define a new phase on the film surface.

The PL emission of the PVA/GQD films exhibits maxima at ~420 nm, ~434 nm and ~495 nm and shows a dependence on both the amount of GQDs incorporated and the film surface morphology. Almost no modification of the PL signal is observed when comparing the films with 0,4%wt GQD and 0,8%wt GQD, which suggest that the GQDs involved in promoting the growth of 3D PVA islands do not contribute to the PL signal. The maxima at ~495 nm, which corresponds to a broader band, experiences a higher increase in intensity compared with the other PL spectral components when the GQD loading is increased above 1,2%wt, and the PL emission saturates and diminishes for the films with 2%wt GQD loads, in correlation with the appearance of the new extended surface phase.

The results revealed in this study provide valuable insights into how the structure and surface morphology of PVA/GQD films influence their photoluminescent (PL) response. This understanding is of paramount importance in advancing and fine-tuning these materials for a wide array of applications, including optoelectronic devices, sensors, nanophotonic technologies. Additionally, knowledge of the impact of the incorporation of GQD on the surface molecular rearrangements of PVA/GQD films is essential for comprehending their potential influence and behavior when employed as imaging agents in biomaterials or as drug delivery careers.

Author Contributions: Conceptualization: G.M.J. and M.T.C; methodology: E.D., G.K., P.H., B.M., S.K. G.M.J. and M.T.C; validation and resources: B.M., S.K., G.M.J. and M.T.C.; formal analysis: E.D., B.R., G.K., P.H. and M.T.C.; investigation and data curation: E.D., B.R, G.K., P.H. and M.T.C.; writing—original draft preparation: E.D. and M.T.C.; writing—review and editing, G.K., P.H., B.M., G.M.J. and M.T.C.; visualization: E.D. and M.T.C.; supervision, project administration and funding acquisition: B.M. and M.T.C. All authors have read and agreed to the published version of the manuscript.

Funding: We acknowledge financial support from under projects: Ref. 2022-GRIN-34226 (Plan Propio UCLM cofunded 85% by FEDER), PID2021-122562NB-I00 (MICINN) and MAD2D-CM-UCM (Comunidad de Madrid, by the Recovery, Transformation and Resilience Plan, and by NextGenerationEU). E. D. acknowledges financial support from ERASMUS+ KA107 (ref. 2017-1-ES01KA107-036732) for a stay at the UCLM in Almadén, Spain. G.K. acknowledges financial support from the UCLM for her stay in Almadén, Spain under contract 2022-UNIVERS-11036, ref. 2022-POST-20987.

Data Availability Statement: The data presented in this study are available on request from the corresponding author.

Acknowledgments: Carlos Rivera Cavanillas (UCLM IRICA Instrumentation Service) is gratefully acknowledged for technical aid in XRD, FT-IR and TGA/DTA data acquisition

Conflicts of Interest: The authors declare no conflict of interest. The funders had no role in the design of the study; in the collection, analyses, or interpretation of data; in the writing of the manuscript, or in the decision to publish the results.

References

1. Park, H.; Hyun Noh, S.; Hye Lee, J.; Jun Lee, W.; Yun Jaung, J.; Geol Lee, S.; Hee Han, T. Large Scale Synthesis and Light Emitting Fibers of Tailor-Made Graphene Quantum Dots. *Scientific Reports* **2015**, *5*, 1-9, doi:10.1038/srep14163.
2. Kausar, A. Technical imprint of polymer nanocomposite comprising graphene quantum dot. *Polymer-Plastics Technology and Materials* **2019**, *58*, 597-617, doi:10.1080/25740881.2018.1563110.
3. Hai, X.; Feng, J.; Chen, X.; Wang, J. Tuning the optical properties of graphene quantum dots for biosensing and bioimaging. *Journal of Materials Chemistry B* **2018**, *6*, 3219-3234, doi:10.1039/c8tb00428e.
4. Barati, F.; Avatefi, M.; Moghadam, N.B.; Asghari, S.; Ekrami, E.; Mahmoudifard, M. A review of graphene quantum dots and their potential biomedical applications. *Journal of Biomaterials Applications* **2022**, *37*, 1137-1158, doi:10.1177/08853282221125311.
5. Kharangarh, P.R.; Rawal, R.; Singh, S.; Bhardwaj, P. Recent Advancement of Luminescent Graphene Quantum Dots for Energy-Related Applications. In *Handbook of Porous Carbon Materials*; Springer: 2023; pp. 147-164.
6. Gobi, N.; Vijayakumar, D.; Keles, O.; Erogbogbo, F. Infusion of graphene quantum dots to create stronger, tougher, and brighter polymer composites. *ACS omega* **2017**, *2*, 4356-4362.
7. Arthisree, D.; Joshi, G.M. Study of polymer Graphene Quantum Dot nanocomposites. *Journal of Materials Science: Materials in Electronics* **2017**, *28*, 10516-10524, doi:10.1007/s10854-017-6825-6.
8. Riccio, B.V.F.; Silvestre, A.L.P.; Meneguin, A.B.; Ribeiro, T.d.C.; Klosowski, A.B.; Ferrari, P.C.; Chorilli, M. Exploiting Polymeric Films as a Multipurpose Drug Delivery System: a Review. *AAPS PharmSciTech* **2022**, *23*, 269.
9. Majeed, Z.; Mubashir, M.; Show, P.L.; Manzoor, E. Biodegradation Study of Polyvinyl Alcohol-Based Biocomposites and Bionanocomposites. *Polyvinyl Alcohol-Based Biocomposites and Bionanocomposites* **2023**, 31-58.
10. Kovalchuk, A.; Huang, K.; Xiang, C.; Martí, A.A.; Tour, J.M. Luminescent Polymer Composite Films Containing Coal-Derived Graphene Quantum Dots. *ACS Applied Materials & Interfaces* **2015**, *7*, 26063-26068, doi:10.1021/acsami.5b06057.
11. Yang, G.; Wan, X.; Liu, Y.; Li, R.; Su, Y.; Zeng, X.; Tang, J. Luminescent Poly(vinyl alcohol)/Carbon Quantum Dots Composites with Tunable Water-Induced Shape Memory Behavior in Different pH and Temperature Environments. *ACS Applied Materials & Interfaces* **2016**, *8*, 34744-34754, doi:10.1021/acsami.6b11476.
12. Rodrigues, B.V.M.; Cabral, T.S.; Sgobbi, L.F.; Delezuk, J.A.M.; Pessoa, R.S.; Triboni, E.R.; de Moraes, T.B.F.; Lobo, A.O. A simple and green method for the production of nanostructured materials from poly(vinyl alcohol)/graphene quantum dots. *Materials Chemistry and Physics* **2018**, *219*, 242-250, doi:https://doi.org/10.1016/j.matchemphys.2018.08.030.
13. Syed Zainol Abidin, S.N.J.; Mamat, S.; Abdul Rasyid, S.; Zainal, Z.; Sulaiman, Y. Fabrication of poly(vinyl alcohol)-graphene quantum dots coated with poly(3,4-ethylenedioxythiophene) for supercapacitor. *Journal of Polymer Science Part A: Polymer Chemistry* **2018**, *56*, 50-58, doi:https://doi.org/10.1002/pola.28859.
14. Wongrerkdee, S.; Pimpang, P. Ultraviolet-shielding and water resistance properties of graphene quantum dots/ polyvinyl alcohol composite-based film. *Journal of Metals, Materials and Minerals* **2020**, *30*, 90-96, doi:10.55713/jmmm.v30i4.722.
15. Fauzi, N.I.M.; Fen, Y.W.; Eddin, F.B.K.; Daniyal, W.M.E.M.M. Structural and Optical Properties of Graphene Quantum Dots−Polyvinyl Alcohol Composite Thin Film and Its Potential in Plasmonic Sensing of Carbaryl. *Nanomaterials* **2022**, *12*, doi:10.3390/nano12224105.
16. Kumar, Y.R.; Deshmukh, K.; Ali, M.M.N.; Abhijay, G.; Al-Onazi, W.A.; Al-Mohaimeed, A.M.; Pasha, S.K.K. Structure, morphology and modelling studies of polyvinylalcohol nanocomposites reinforced with nickel oxide nanoparticles and graphene quantum dots. *Environmental Research* **2022**, *203*, 111842, doi:https://doi.org/10.1016/j.envres.2021.111842.
17. Wang, T.; Yang, F.; Zhang, L.; Tang, Z.; Liu, W.; Zhong, L.; He, Z.; Chai, S. Fluorescence Quenching and Highly Selective Adsorption of Ag+ Using N-Doped Graphene Quantum Dots/Poly(vinyl alcohol) Composite Membrane. *Industrial & Engineering Chemistry Research* **2022**, *61*, 18090-18099, doi:10.1021/acs.iecr.2c03453.
18. Afkhami, H.; Oskouie, I.M.; Mohammadi, L.; Dezfuli, A.S. Organic Dots-PVA as a Platform for Wound Dressing. **2023**, doi:10.21203/rs.3.rs-2572037/v1.
19. Badry, R.; Ibrahim, A.; Gamal, F.; Elhaes, H.; Yahia, I.S.; Zahran, H.Y.; Zahran, M.; Abdel-Wahab, M.S.; Zyoud, S.H.; Ibrahim, M.A. Design and implementation of low-cost gas sensor based on functionalized

graphene quantum dot/Polyvinyl alcohol polymeric nanocomposites. *Optical and Quantum Electronics* **2023**, *55*, doi:10.1007/s11082-022-04510-0.

20. Belko, N.V.; Chizhevsky, V.N.; Parkhats, M.V.; Lepeshkevich, S.V.; Kulahava, T.A.; Mogilevtsev, D.S. Single-Photon Spectroscopy and Emission Statistics of Graphene Quantum Dots in Organic Structures. *Journal of Applied Spectroscopy* **2023**, *90*, 316-324, doi:10.1007/s10812-023-01538-2.
21. Du, J.; Zhu, W.; She, X.; Yu, Q.; Yang, Q.; Zhang, D.; Chen, J. A robust and fluorescent nanocomposite hydrogel with an interpenetrating polymer network based on graphene quantum dots. *Polymer Engineering & Science* **2023**, *63*, 2169-2179, doi:10.1002/pen.26354.
22. Wan, Y.; Yao, L.; Cui, P. Graphene quantum dots doped poly (vinyl alcohol) hybrid membranes for Desalination via Pervaporation. *Chinese Journal of Chemical Engineering* **2023**.
23. Cuberes, M.T. Atomic force microscopy manipulation with ultrasonic excitation. *Journal of Physics: Conference Series* **2008**, *100*, doi:10.1088/1742-6596/100/5/052013.
24. Assender, H.E.; Windle, A.H. Crystallinity in poly(vinyl alcohol). 1. An X-ray diffraction study of atactic PVOH. *Polymer* **1998**, *39*, 4295-4302, doi:https://doi.org/10.1016/S0032-3861(97)10296-8.
25. Assender, H.E.; Windle, A.H. Crystallinity in poly(vinyl alcohol) 2. Computer modelling of crystal structure over a range of tacticities. *Polymer* **1998**, *39*, 4303-4312, doi:https://doi.org/10.1016/S0032-3861(97)10297-X.
26. Hashemzadeh, N.; Hasanzadeh, M.; Shadjou, N.; Eivazi-Ziaei, J.; Khoubnasabjafari, M.; Jouyban, A. Graphene quantum dot modified glassy carbon electrode for the determination of doxorubicin hydrochloride in human plasma. *Journal of Pharmaceutical Analysis* **2016**, *6*, 235-241, doi:https://doi.org/10.1016/j.jpha.2016.03.003.
27. Kumar, S.; Ojha, A.K.; Ahmed, B.; Kumar, A.; Das, J.; Materny, A. Tunable (violet to green) emission by high-yield graphene quantum dots and exploiting its unique properties towards sun-light-driven photocatalysis and supercapacitor electrode materials. *Materials Today Communications* **2017**, *11*, 76-86, doi:https://doi.org/10.1016/j.mtcomm.2017.02.009.
28. Anicuta, S.-G.; Dobre, L.; Stroescu, M.; Jipa, I. Fourier transform infrared (FTIR) spectroscopy for characterization of antimicrobial films containing chitosan. *Analele Universită Ńii din Oradea Fascicula: Ecotoxicologie, Zootehnie şi Tehnologii de Industrie Alimentară* **2010**, *2010*, 1234-1240.
29. Tretinnikov, O.N.; Zagorskaya, S.A. Determination of the degree of crystallinity of poly(vinyl alcohol) by FTIR spectroscopy. *Journal of Applied Spectroscopy* **2012**, *79*, 521-526, doi:10.1007/s10812-012-9634-y.
30. Huang, S.; Qiu, H.; Zhu, F.; Lu, S.; Xiao, Q. Graphene quantum dots as on-off-on fluorescent probes for chromium(VI) and ascorbic acid. *Microchimica Acta* **2015**, *182*, 1723-1731, doi:10.1007/s00604-015-1508-6.
31. Chen, T.; Wu, Z.; Wei, W.; Xie, Y.; Wang, X.; Niu, M.; Wei, Q.; Rao, J. Hybrid composites of polyvinyl alcohol (PVA)/Si–Al for improving the properties of ultra-low density fiberboard (ULDF). *RSC Advances* **2016**, *6*, 20706-20712, doi:10.1039/C5RA26868K.
32. Fomo, G.; Achadu, O.J.; Nyokong, T. One-pot synthesis of graphene quantum dots–phthalocyanines supramolecular hybrid and the investigation of their photophysical properties. *Journal of Materials Science* **2018**, *53*, 538-548, doi:10.1007/s10853-017-1539-y.
33. Jaipakdee, N.; Pongjanyakul, T.; Limpongsa, E. Preparation and characterization of poly (vinyl alcohol)-poly (vinyl pyrrolidone) mucoadhesive buccal patches for delivery of lidocaine HCL. *Int. J. Appl. Pharm* **2018**, *10*, 115-123.
34. Mallapragada, S.K.; Peppas, N.A.; Colombo, P. Crystal dissolution-controlled release systems. II. Metronidazole release from semicrystalline poly(vinyl alcohol) systems. *Journal of Biomedical Materials Research* **1997**, *36*, 125-130, doi:https://doi.org/10.1002/(SICI)1097-4636(199707)36:1<125::AID-JBM15>3.0.CO;2-H.
35. Mansur, H.S.; Sadahira, C.M.; Souza, A.N.; Mansur, A.A.P. FTIR spectroscopy characterization of poly (vinyl alcohol) hydrogel with different hydrolysis degree and chemically crosslinked with glutaraldehyde. *Materials Science and Engineering: C* **2008**, *28*, 539-548, doi:https://doi.org/10.1016/j.msec.2007.10.088.
36. Abureesh, M.A.; Oladipo, A.A.; Gazi, M. Facile synthesis of glucose-sensitive chitosan–poly(vinyl alcohol) hydrogel: Drug release optimization and swelling properties. *International Journal of Biological Macromolecules* **2016**, *90*, 75-80, doi:https://doi.org/10.1016/j.ijbiomac.2015.10.001.
37. Alghunaim, N.S. Optimization and spectroscopic studies on carbon nanotubes/PVA nanocomposites. *Results in Physics* **2016**, *6*, 456-460, doi:https://doi.org/10.1016/j.rinp.2016.08.002.
38. Thomas, D.; Cebe, P. Self-nucleation and crystallization of polyvinyl alcohol. *Journal of Thermal Analysis and Calorimetry* **2017**, *127*, 885-894, doi:10.1007/s10973-016-5811-1.
39. Liu, P.; Chen, W.; Liu, C.; Tian, M.; Liu, P. A novel poly (vinyl alcohol)/poly (ethylene glycol) scaffold for tissue engineering with a unique bimodal open-celled structure fabricated using supercritical fluid foaming. *Scientific Reports* **2019**, *9*, doi:10.1038/s41598-019-46061-7.
40. Holland, B.J.; Hay, J.N. The thermal degradation of poly(vinyl alcohol). *Polymer* **2001**, *42*, 6775-6783, doi:10.1016/s0032-3861(01)00166-5.

41. Pandey, S.; Pandey, S.K.; Parashar, V.; Mehrotra, G.K.; Pandey, A.C. Ag/PVA nanocomposites: optical and thermal dimensions. *Journal of Materials Chemistry* **2011**, *21*, 17154-17159, doi:10.1039/C1JM13276H.
42. Gomaa, M.M.; Hugenschmidt, C.; Dickmann, M.; Abdel-Hady, E.E.; Mohamed, H.F.M.; Abdel-Hamed, M.O. Crosslinked PVA/SSA proton exchange membranes: correlation between physiochemical properties and free volume determined by positron annihilation spectroscopy. *Physical Chemistry Chemical Physics* **2018**, *20*, 28287-28299, doi:10.1039/C8CP05301D.
43. Nakajima, H.; Wang, Z.M.; Strawhecker, K.; Manias, E. Effect of nm-Thin Inorganic Layered Fillers on the Crystallization of Polymer Nanocomposites. *MRS Proceedings* **2003**, *791*, doi:10.1557/proc-791-q4.10.
44. Strawhecker, K.E.; Manias, E. AFM of Poly(vinyl alcohol) Crystals Next to an Inorganic Surface. *Macromolecules* **2001**, *34*, 8475-8482, doi:10.1021/ma0101862.
45. Im, M.J.; Kim, J.I.; Hyeong, S.K.; Moon, B.J.; Bae, S. From Pristine to Heteroatom-Doped Graphene Quantum Dots: An Essential Review and Prospects for Future Research. *Small* **2023**, 2304497.
46. Sheikh Mohd Ghazali, S.A.I.; Fatimah, I.; Zamil, Z.N.; Zulkifli, N.N.; Adam, N. Graphene quantum dots: A comprehensive overview. *Open Chemistry* **2023**, *21*, doi:10.1515/chem-2022-0285.